ELSEVIER

Ocean Modelling 4 (2002) 327–345

Ocean Modelling

www.elsevier.com/locate/omodol

Sensitivity of a double-gyre ocean model to details of stochastic forcing

Philip Sura [a,*], Cécile Penland [b]

[a] *Meteorologisches Institut der Universität Hamburg, Germany*
[b] *NOAA-CIRES/Climate Diagnostics Center, Boulder, CO, USA*

Abstract

As the importance of stochastic forcing to the interdecadal variability in the ocean and atmosphere becomes more widely appreciated, numerical stochastic modeling becomes more common. In most cases, the details of how the stochastic modeling is implemented are not considered an important part of the modeling. In this study, we show in the context of a reduced gravity, double-gyre ocean model driven by wind stress how "minor" details of stochastic forcing can have a significant effect on the temporal and spatial response by the forced system.

Keywords: Wind-driven circulation; Numerical modeling; Stochastic models; Oceanic response to atmospheric forcing; Wind-induced variability

1. Introduction

The effect of stochastic "weather" noise on the oceanic "climate" system has been an object of research since Hasselmann's classic paper appeared in 1976. That paper emphasized univariate linear systems which have been surprisingly successful in describing, for example, mid-latitude sea surface temperature (e.g., Frankignoul and Hasselmann, 1977; Blaauboer et al., 1982). The success of these studies has inspired researchers to consider stochastic forcing as a possible source of more complex dynamics, particularly on the interdecadal scale (e.g., Barnett et al., 1999; Junge et al., 2000; Czaja and Frankignoul, 1999; Weng and Neelin, 1998; Sura et al., 2000, 2001; Münnich et al., 1998; Saravanan and McWilliams, 1997, 1998; Mikolajewicz and Maier-Reimer, 1990, and others).

* Corresponding author. Present address: Scripps Institution of Oceanography, University of California, San Diego, 9500 Gilman Drive, La Jolla, CA 92093-0230, USA. Tel.: +1-858-822-5051; fax: +1-858-534-9820.
E-mail address: pgsura@ucsd.edu (P. Sura).

1463-5003/02/$ - see front matter
PII: S1463-5003(02)00008-2

The physical justification of stochastic forcing lies in the dynamical form of the central limit theorem (CLT: e.g., Papanicolaou and Kohler, 1974; Gardiner, 1985), which states the conditions under which rapidly varying, generally nonlinear processes may be treated as white or colored Gaussian random noise. The treatment of these processes as noise is not arbitrary but is rather strictly prescribed by the CLT. Nevertheless, the implementation of stochastic forcing in climate models seems to be nearly as varied as the climate models themselves. Although most researchers appear to use some type of autoregression process to model the noise, the details of the implementation, such as the frequency of sampling the process, vary widely and are sometimes not even included in the description of the model. This is true in spite of the large literature on dynamically consistent numerical methods of treating stochastic processes (e.g., Rümelin, 1982; Kloeden and Platen, 1992). This widespread lack of attention to the details of the temporal specification is somewhat puzzling. After all, the importance of *spatial* variations in stochastic forcing to system response is well known, and has been investigated in many studies (e.g., Farrell and Iaonnou, 1996a,b; Penland and Matrosova, 1994; Penland and Sardeshmukh, 1995; Sura et al., 2000, 2001; Junge et al., 2000; Moore, 1999), some of which also address the temporal aspects of stochastic modeling. Nevertheless, it may appear reasonable that these details would not be important as long as the timescales of interest in the forced system are much longer than those of the stochastic driving.

The apparent reasonableness of this assertion led us to investigate this notion. In this paper, it is shown how different descriptions of small timescale aspects of stochastic forcing can cause significant variations in the low-frequency response of a simple but oceanographically relevant double-gyre model. The double-gyre model has been used extensively to investigate various linear and nonlinear effects of wind stress forcing on the oceanic circulation (e.g., Pedlosky, 1996). Beside the role played by dissipative processes within the western boundary currents, the rich structure of multiple equilibria is becoming evident. Several authors show that, for a range of parameters, the double-gyre circulation possesses multiple steady states (e.g., Cessi and Ierley, 1995; Speich et al., 1995; Jiang et al., 1995; Primeau, 1998a,b; Scott and Straub, 1998). More precisely, these authors explicitly computed fixed point solutions for a broad range of parameters except Jiang et al. (1995). Jiang et al. (1995) do not explicitly compute stationary solutions, but use a time-dependent model to explore a parameter range where even a time-stepping procedure yields steady-state solutions. The quasi-geostrophic double-gyre (Cessi and Ierley, 1995; Primeau, 1998a,b; Scott and Straub, 1998) is characterized by two classes of steady states: one class consists of perfectly antisymmetric solutions and the other class consists of asymmetric solutions. The asymmetric solutions come in pairs due to the quasi-geostrophic symmetry. Cessi and Ierley (1995) conjecture that all equilibria are of significance in the description of the low-frequency variability of the wind-driven circulation, regardless of their stability. Comparable experiments with the primitive equations were performed by Speich et al. (1995) and Jiang et al. (1995). Despite the fact that the primitive equations do not satisfy quasi-geostrophic symmetry, they showed that the asymmetric equilibria come in pairs, in agreement with the quasi-geostrophic calculations.

The impact of an additive stochastic wind forcing on the double-gyre circulation is studied, for example, by Griffa and Castellari (1991), Moore (1999), and Sura et al. (2001). Thereby, the stochastic wind stress components are interpreted as high-frequency weather fluctuations of the mid-latitude atmosphere. Griffa and Castellari (1991) analyze the effects of the stochastic wind

stress on the climatological mean of the highly nonlinear ocean circulation. It is found that the stochastic wind drives the circulation toward a Fofonoff type flow, as long as only the stochastic forcing is used. In the case of an additional steady double-gyre wind stress, the stochastic component is found to weaken the recirculation regions and the jet between the two gyres. This change of the mean can be described in terms of a "noise-induced transition" (Horsthemke and Lefever, 1984). Noise-induced transitions can occur if a certain amount of randomness is present in the environment of the nonlinear system under consideration. Then, the system undergoes a characteristic qualitative change of its probability density function (PDF) due to the impact of the external noise. Moore (1999) uses the barotropic double-gyre model to compute stochastic optimals. In this case stochastic optimals are spatial patterns of stochastic wind stress curl that are optimal for increasing the variability of the double-gyre ocean model. The gravest stochastic optimal is reminiscent of the Ekman pumping produced by transient large-scale atmospheric pressure systems. That is, Moore (1999) shows that the storm track has the potential to produce significant variability in the subtropical and subpolar gyres. Sura et al. (2001) introduce a spatially inhomogeneous stochastic component to parameterize the observed localized variability of the midlatitude storm-tracks. The authors show that the simple wind-driven ocean model forced by a combination of a double-gyre wind stress and a spatially inhomogeneous stochastic field shows a complex behaviour. The dominant regime is a quasi-antisymmetric state with a free jet penetrating deep into the basin. A second flow pattern appears to be related to the choice of the spatially inhomogeneous stochastic forcing. It is asymmetric with a very strong northern recirculation gyre and a north-eastward flowing jet. The asymmetric regime may be related to one member of a known asymmetric pair of stationary solutions found in the deterministic case. The asymmetric pattern does not appear without the spatially inhomogeneous stochastic forcing nor with spatially homogeneous stochastic forcing. Thus, the regime transitions are induced by the spatial inhomogeneity of the white noise variance. Please note that we use the term "regime transition" loosely; there is some doubt as to whether the stable steady states of the deterministic case are able to retain their stability in the presence of stochastic forcing (see below).

In the present study the experimental setup of Sura et al. (2001) is used to investigate how different descriptions of the stochastic forcing can alter the low-frequency response of a simple double-gyre model. We have chosen this setup for the single reason that it has been used so often in the studies cited above. We do not mean to imply that the stochastic forcing is the only problematic issue with this model; however, it is the issue we choose to emphasize. This paper is arranged as follows. In Section 2, a brief description of the ocean model and the atmospheric forcing are provided. The various experiments are explained in Section 3. Results are presented in Section 4, and a general discussion ends this paper.

2. The model

2.1. Ocean model

The nonlinear reduced-gravity equations in transport form are used to model the upper ocean in a rectangular basin of 2400 km by 2400 km extent; (x, y)-coordinates increasing eastward and northward are used. In the reduced-gravity approximation the ocean is represented by a single

active layer of constant density ρ_1 of thickness H. The upper-layer is assumed to overlie a deep and motionless layer of density ρ_2. With this constraint only the first baroclinic mode is modeled. That is, the interface between the two layers represents the permanent thermocline. The eastward and northward transport is defined as $U = uH$ and $V = vH$, whereby u and v are the corresponding velocities, τ^x and τ^y are the wind stress components, g is the acceleration of gravity, and f is the Coriolis parameter given by the β-plane approximation, $f = f_0 + \beta y$. Thus, the equations are:

$$\frac{\partial U}{\partial t} + \frac{\partial}{\partial x}\left(\frac{U^2}{H}\right) + \frac{\partial}{\partial y}\left(\frac{UV}{H}\right) - fV = \frac{-g'}{2}\frac{\partial H^2}{\partial x} + \frac{\tau^x}{\rho_1} - rU + A\Delta U, \tag{1}$$

$$\frac{\partial V}{\partial t} + \frac{\partial}{\partial x}\left(\frac{UV}{H}\right) + \frac{\partial}{\partial y}\left(\frac{V^2}{H}\right) + fU = \frac{-g'}{2}\frac{\partial H^2}{\partial y} + \frac{\tau^y}{\rho_1} - rV + A\Delta V, \tag{2}$$

$$\frac{\partial H}{\partial t} + \frac{\partial U}{\partial x} + \frac{\partial V}{\partial y} = 0, \tag{3}$$

where the reduced gravity is $g' = g(\rho_2 - \rho_1)/\rho_2$.

Interfacial friction is parameterized by Rayleigh friction scaled by r; the lateral viscosity is represented by a Laplacian scaled by A. All parameters of the model are summarized in Table 1. For dynamical parameters, standard numerical values are used. The Laplacian friction coefficient is chosen to adjust the width of the dimensional Munk layer $\delta_M^* = (A/\beta)^{1/3}$ to approximately the width of the numerical grid: $\delta_M^* = 23.11$ km and $\Delta x = \Delta y = 20$ km (see below).

The dynamics of the wind-driven model is controlled by several nondimensional parameters. The parameters, derived from the nondimensional form of the barotropic quasi-geostrophic vorticity equation (e.g., Pedlosky, 1996), are the dimensional inertial, Stommel, and Munk layer thickness scaled by the width of the basin (the asterisk denotes dimensional values)

$$\delta_I = \frac{\delta_I^*}{L_x} = \left(\frac{U}{\beta L_x^2}\right)^{1/2}, \quad \delta_S = \frac{\delta_S^*}{L_x} = \frac{r}{\beta L_x}, \quad \delta_M = \frac{\delta_M^*}{L_x} = \left(\frac{A}{\beta L_x^3}\right)^{1/3}. \tag{4}$$

Table 1
Model parameters

Coriolis parameter	$f = 1.03 \times 10^{-4}$ s^{-1}
Beta-effect	$\beta = 1.62 \times 10^{-11}$ m^{-1} s^{-1}
Upper-layer equilibrium depth	$H_0 = 600$ m
Rayleigh friction coefficient	$r = 1 \times 10^{-7}$ s^{-1}
Laplacian friction coefficient	$A = 2 \times 10^2$ m^2 s^{-1}
Upper-layer density	$\rho_1 = 1027$ kg m^{-3}
Lower-layer density	$\rho_2 = 1030$ kg m^{-3}
Reduced gravity	$g' = 0.029$ m s^{-2}
Wind stress amplitude	$\tau_0 = 0.05$ N m^{-2}
Time-step	$\Delta t = 1200$ s
Domain extent (north–south)	$L_y = 2400$ km
Domain extent (east–west)	$L_x = 2400$ km
Grid resolution	$\Delta x = 20$ km
	$\Delta y = 20$ km

The velocity scale in the interior, U, and a characteristic value of the wind stress, τ, are connected by the Sverdrup relation. For a rectangular basin with a double-gyre wind stress, the scaling reads $U = (2\pi\tau)/(\rho_1 \beta L_y H_0)$ (then τ is the amplitude of the double-gyre forcing). The three parameters measure the importance of the nonlinearity, bottom friction, and lateral diffusion. In particular, the relative importance of the nonlinearity and the lateral diffusion is often expressed through the boundary layer Reynolds number

$$Re = \left(\frac{\delta_I}{\delta_M} \right)^3. \tag{5}$$

For the parameters used in the present study (Table 1) the dimensional Stommel and Munk layer widths are $\delta_S^* = 6.17$ km and $\delta_M^* = 23.11$ km (nondimensional values: $\delta_S = 2.571 \times 10^{-3}$, $\delta_M = 9.629 \times 10^{-3}$). For a typical wind stress value of 0.05 N m^{-2} the dimensional inertial layer width is $\delta_I^* = 28.44$ km (nondimensional value: $\delta_I = 1.185 \times 10^{-2}$). This gives a boundary layer Reynolds number of $Re = 1.86$. The equations of motion are solved numerically on a staggered Arakawa-C grid. The model resolution is 20 km in both the zonal and meridional direction. Note that the Stommel layer has a width of $\delta_S^* = 6.17$ km and, therefore, is not resolved within the used resolution. Time differencing is performed by the Matsuno (Euler backward) scheme, space differencing by space-centered finite difference approximations. The time-step is 20 min. The nonlinear advection terms are computed by first averaging the prognostic variables in space to calculate the required products at the appropriate meshpoints before the centered finite are calculated. The no-flux boundary condition is used to suppress the normal flow at the boundaries. Furthermore, the tangential boundary condition is a linear combination of tangential velocity and stress

$$(\gamma \vec{u} \cdot \vec{t} + (1-\gamma)\vec{n} \cdot \nabla(\vec{u} \cdot \vec{t}))|_C = 0, \tag{6}$$

where $\vec{t}$ is the unit vector tangent to the domain boundary C and $\vec{n}$ is the unit vector normal to C. The parameter γ has the limiting values for no-slip ($\gamma = 1$) and free-slip ($\gamma = 0$) boundary conditions. For this reason, (6) is normally designated as a partial-slip boundary condition. For this study a half-slip condition ($\gamma = 0.5$) is employed. The choice of the half-slip condition is due to Haidvogel et al. (1992), who suggests that the tangential velocities at the boundaries should lie between the no-slip and the free-slip limits.

Two standard definitions are introduced that are used throughout the remainder of this paper. The layer thickness H is the sum of the equilibrium depth H_0 and the depth anomaly h, so that $H(x,y,t) = H_0 + h(x,y,t)$. Furthermore, all time-dependent variables, e.g., ψ, are divided into a long-term mean $\overline{\psi}$ and a deviation ψ', such that $\psi = \overline{\psi} + \psi'$.

2.2. Atmospheric forcing

The atmospheric forcing of the ocean by the wind stress consists of a mean field and a stochastic field

$$\vec{\tau} = \vec{\tau}_{\text{mean}} + \vec{\tau}_{\text{stochastic}}. \tag{7}$$

The mean wind stress $\vec{\tau}_{\text{mean}}$ is represented by a zonal wind field with a sinusoidal pattern

$$\tau^x_{\text{mean}} = \phi\tau_0 \cos\left(\frac{2\pi y}{L_y}\right), \quad -\frac{L_y}{2} \leqslant y \leqslant \frac{L_y}{2}. \tag{8}$$

This generates a northern cyclonic subpolar and a southern anticyclonic subtropical gyre. The reference wind stress amplitude τ_0 is set to a standard value of 0.05 N m^{-2}. Recognize that the amplitude of the fluid motion and hence the nonlinearity of the system is proportional to the strength of the wind stress. Therefore, nonlinear effects can be studied by varying the wind stress parameter ϕ. Because the boundary layer Reynolds number for the reference wind stress amplitude τ_0 is $Re = 1.86$, the value of Re for different wind stress parameters is $Re = 1.86\phi^{3/2}$.

The spatially inhomogeneous stochastic forcing $\vec{\tau}_{\text{stochastic}}$ accounts for the mid-latitude synoptic atmospheric variability and is parameterized by the bulk formula for the wind stress. This leads to the parameterization of the spatially inhomogeneous stochastic forcing

$$\begin{aligned}
&\vec{\tau}_{\text{stochastic}} = \rho_{\text{Air}} C_{\text{D}} |\vec{u}'| \vec{u}', \\
&u'(x,y,t) = \eta_x(t) f(x,y), \\
&v'(x,y,t) = \eta_y(t) f(x,y),
\end{aligned} \tag{9}$$

where ρ_{Air}, $|\vec{u}'|$ and $\vec{u}'$ are the air density (1.3 kg m^{-3}), near surface wind speed, and velocity; C_{D} (2×10^{-3}) is the drag coefficient, and $\eta_{x,y}(t)$ are independent stochastic processes with zero mean and standard deviation σ. The weight function $f(x,y)$ parameterizes the spatial structure of the atmospheric variability by a Gaussian shape, whose origin is placed in the center of the basin

$$f(x,y) = \frac{\alpha}{\left(\pi\lambda_x\lambda_y \text{Erf}(L_x/2\lambda_x)\text{Erf}(L_y/2\lambda_y)\right)^{1/2}} \exp\left(-\frac{x^2}{2\lambda_x^2} - \frac{y^2}{2\lambda_y^2}\right) \tag{10}$$

with the error function Erf. The denominator normalizes the area integral of the squared weight function over the basin domain Ω to unity, and α is a scaling constant. The inhomogeneity parameters, λ_x and λ_y, control the spatial structure of the atmospheric variability. To obtain circular symmetry of the stochastic forcing, $\lambda_x = \lambda_y = \lambda$. The Gaussian shape with circular symmetry is chosen for convenience to parameterize the localized atmospheric eddy activity along the storm-tracks in a conceptual manner. The physical motivation for the particular weight function is that the observed climatological position of the North Atlantic storm-track maximum is approximately coincident with that of the observed mean zero wind stress curl line The low-frequency meridional shift of the storm track due to NAO is not included in the parameterization used.

The scaling constant α is chosen to adjust the weight function in the origin to 1 for $\lambda = 600$ km. Thus, $\alpha = (\pi\lambda_x\lambda_y \text{Erf}(L_x/2\lambda_x)\text{Erf}(L_y/2\lambda_y))^{1/2}$ with $\lambda_x = \lambda_y = 600$ km. The variance σ^2 of the stochastic forcing is 25 m^2 s^{-2} (except one experiment; see following section), characterizing the observed atmospheric conditions in the North Atlantic region. That is, the variance of the wind speed in the center of the basin is comparable to the observed conditions (Wright, 1988). Nevertheless, the stochastic forcing has to be understood as a conceptual tool to study the effect of noise on simple wind-driven ocean models. In the following experiments we consider only the cases where $\phi = 1.3$ and $\lambda = 300$ km. Then, the corresponding boundary layer Reynolds number is $Re = 2.76$ and the stochastic forcing is spatially very inhomogeneous. Moreover, with $\phi = 1.3$

the maximum of the double-gyre wind speed is 5 m s^{-1}. That is, the mean and the stochastic forcing have the same magnitude.

These are the parameter values where Sura et al. (2001) find very pronounced transitions between a quasi-antisymmetric and an asymmetric flow pattern. This situation is chosen as a reference case, because the oceanic response to the spatially inhomogeneous stochastic forcing is well defined in time and space and already documented (Sura et al., 2001). In the following, only the small-timescale aspects of the stochastic forcing are changed, as described in the following section.

3. Experiments

There are two issues to be considered: the temporal covariance structure and the probability distribution of the rapidly varying forcing. These issues are addressed using four forms of stochastic driving. The first (Model 1) is that of Sura et al. (2000, 2001), who sampled a flat distribution once daily. For a flat distribution with zero mean and variance $\sigma^2 = (2\eta_0)^2/12$ the probability density dP is constant over the interval $[-\eta_0, \eta_0]$ (see Appendix A). Once daily means that the noise is updated once a day. The forcing in the second experiment (Model 2) was also sampled once daily, but from a Gaussian probability distribution with the same variance as that of the forcing in Model 1. The third experiment (Model 3) consisted of forcing the ocean model with Gaussian red noise having a decay time of 1 day, but sampled at each 20-min time-step during the model integration. That is, the lagged autocorrelation function for the stochastic forcing in Models 1 and 2 is equal to unity for lags less than one day, but is equal to zero for lags greater than one day. The autocorrelation function for the stochastic forcing in Model 3 decays exponentially with an e-folding time of one day. Models 2 and 3 are constructed so that their Gaussian distribution has the same variance as the flat distribution of Model 1. The spectra of the different stochastic models are derived in Appendix A and shown in Fig. 1. Recall that spectra are averaged quantities and, therefore, the spectra of Models 1 and 2 are identical. Moreover, it is important to recognize that the spectrum of Model 3 has a higher variability above the e-folding timescale of one day than the spectrum of Model 1 or Model 2. That is, the daily sampling of the

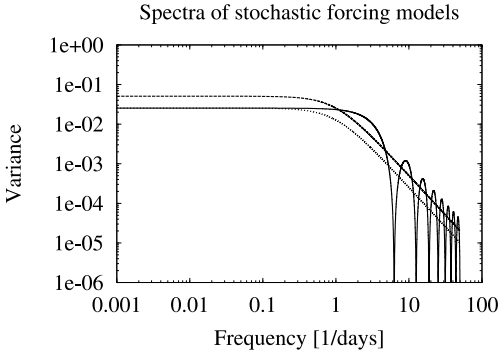

Fig. 1. Variance spectra of the different stochastic forcing models. The spectra of Model 1 (flat distribution sampled once daily) and Model 2 (Gaussian distribution sampled once daily) are indicated by the solid line. The spectrum of Model 3 (Gaussian red noise) is indicated by the long dashed line, whereas the spectrum of Model 4 (Gaussian red noise with decreased variance) is indicated by the short dashed line.

stochastic wind forcing results in a reduced variance of the wind stress above the decorrelation timescale. Because of this a fourth experiment (Model 4), similar to Model 3, but with the total variance reduced to 12.5 m^2 s^{-2} is performed (see Fig. 1). The halving of the variance has the effect that the low-frequency part above the decorrelation timescale of Model 4 coincides with the spectra of Models 1 and 2.

The red-noise forcing in Models 3 and 4 was generated in a manner consistent with a univariate Ornstein–Uhlenbeck process

$$d\eta = -\gamma\eta\,dt + \sqrt{Q}\,dW, \tag{11}$$

where η is the stochastic forcing for Model 3, $\gamma = 1$ day^{-1}, and W is a Wiener process. The Ornstein–Uhlenbeck process, also called red-noise or damped Brownian motion, is one of the simplest stochastic processes. The classical Brownian motion problem describes the irregular motion of a particle immersed in a fluid; the collisions with the fluid particles impart a random force and a viscous drag on the immersed particle (see e.g., Paul and Baschnagel, 1999). Nevertheless, the Ornstein–Uhlenbeck process can also be used to model the high-frequency weather fluctuations of the mid-latitude atmosphere.

The constant Q has been chosen using the fluctuation dissipation relation (FDR: e.g., Penland and Matrosova, 1994):

$$Q = 2\gamma\langle\eta^2\rangle \tag{12}$$

for the specified value of $\langle\eta^2\rangle$. The FDR relates the variance of the stochastic fluctuations to the magnitude of the dissipation. Therefore, the autocorrelation function for the stochastic forcing in Model 3 reads

$$\langle\eta(t)\eta(t')\rangle = \frac{Q}{2\gamma}\exp(-\gamma|t-t'|). \tag{13}$$

The numerical implementation of (11) was performed using the stochastic first-order Runge–Kutta scheme with time-step Δt (Rümelin, 1982; Kloeden and Platen, 1992):

$$\eta(t+\Delta t) = \eta(t) - \gamma\eta\Delta t + \sqrt{Q\Delta t}R, \tag{14}$$

where R is a centered Gaussian random deviate with unit variance. Note that the decay term is updated by the time-step while the random source term is updated by the square root of the time-step. This procedure is necessary to generate a time-series which obeys the FDR (12) and which also has the spectrum appropriate to the dynamical process (11). A test of the numerical model (14) using $\Delta t = 20$ min verified that it generated the desired statistics with sufficient accuracy.

All experiments commence from a resting state and are integrated for 510 years. The first 10 years are always skipped to account for the spin-up phase. Transports, velocities, and depth anomalies are saved once a day. For all further diagnostics monthly means are used to calculate the basin-integrated eddy kinetic energies (see below) because it is reasonable to employ the period of the nondispersive first baroclinic Rossby mode in mid-latitudes as an appropriate timescale, which has the order of years.

A convenient overall description of the transient behaviour of the basin circulation can be given in terms of the integrated eddy energy content in the basin domain Ω. The basin integrated eddy kinetic and eddy potential energies are defined by

$$[E'_{\mathrm{kin}}]_{\Omega} = \frac{1}{\Omega}\int\int_{\Omega}\left(\frac{\rho_1 \bar{H}}{2}(u'^2 + v'^2)\right)\mathrm{d}x\,\mathrm{d}y, \tag{15}$$

$$[E'_{\mathrm{pot}}]_{\Omega} = \frac{1}{\Omega}\int\int_{\Omega}\left(\frac{g'\rho_1 h'^2}{2}\right)\mathrm{d}x\,\mathrm{d}y. \tag{16}$$

The brackets with the Ω subscript denote the basin average. Furthermore, the volume transport stream function ψ is used to show the structure of the flow patterns: $U = -\partial\psi/\partial y, V = \partial\psi/\partial x$. This is done to emphasis the symmetry properties of the double-gyre solutions.

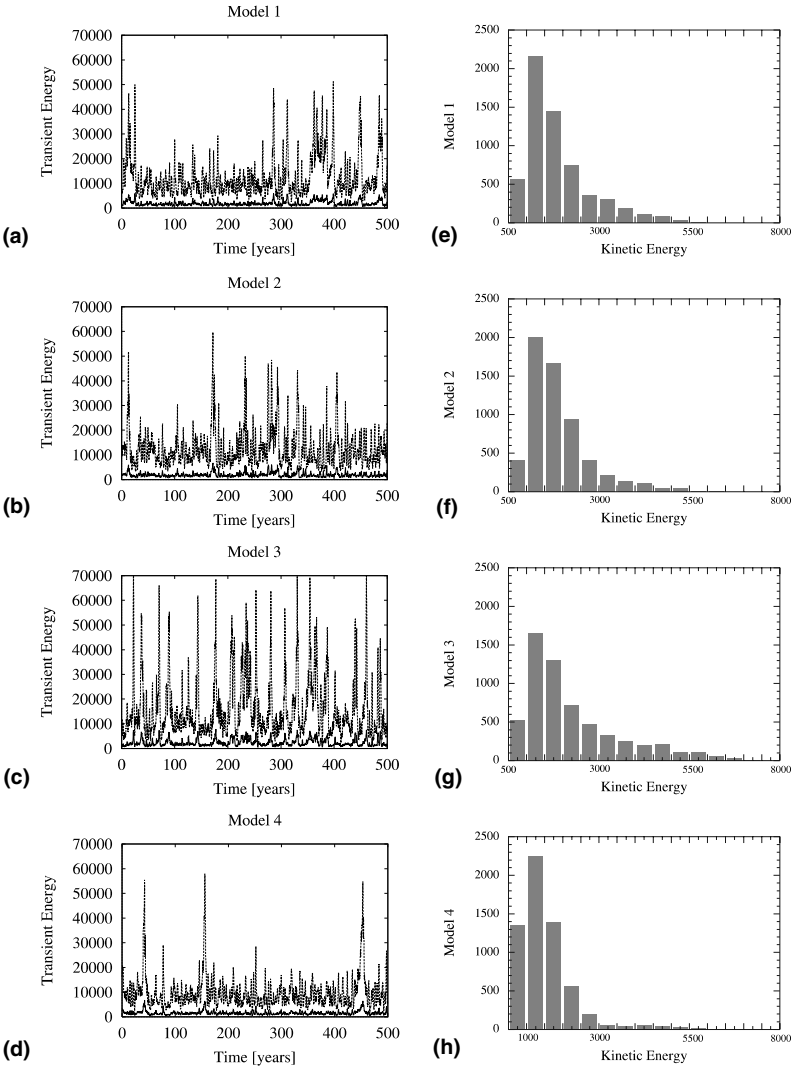

Fig. 2. (a)–(d) Time-series of basin integrated eddy energies (J m^{-2}) for $\phi = 1.3$ for Models 1, 2, 3, and 4 respectively. The dashed lines denote the eddy potential energies, the solid lines the eddy kinetic energies. (e)–(h) The corresponding histograms of the eddy kinetic energies.

4. Results

The time-series of the basin-integrated eddy energies of the four different stochastic models, along with the corresponding histograms of eddy kinetic energy, are shown in Fig. 2. Since histograms of potential energy and kinetic energy show the same qualitative structure, we concentrate on only one of them (kinetic energy) for clarity. In the following, the basic experiments (Models 1–3) are discussed first. The remaining experiment (Model 4) is discussed separately since differences between results from Model 3 and those from Model 4 are caused simply by a change of parameter rather than a change of technique.

4.1. Models 1–3

The common feature in the oceanic response in all the stochastic models is, disregarding the obvious differences discussed later, that the model undergoes transitions between a quasi-anti-

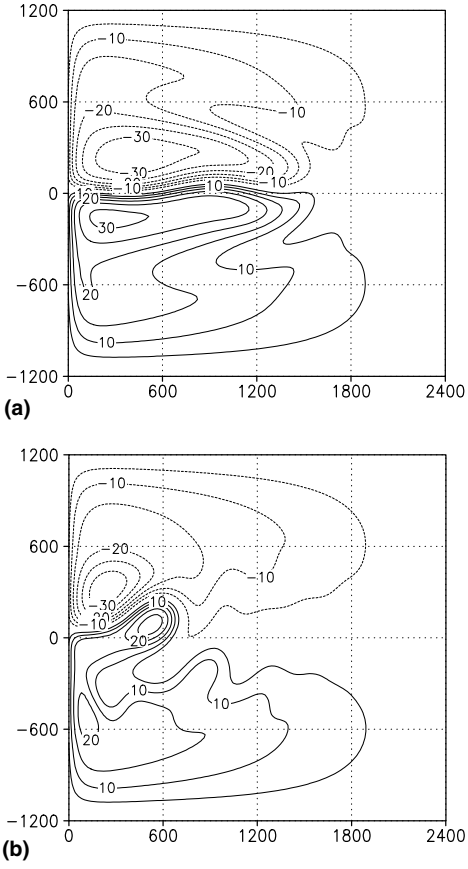

Fig. 3. Representative volume transport streamfunction fields (10^6 m^3 s^{-1}) for the two different regimes in the experiment with $\phi = 1.3$ and $\lambda = 300$ km: (a) represents the low eddy energy state and (b) the high eddy energy state. The axes are horizontal distances in kilometers.

symmetric and a asymmetric flow pattern, as described by Sura et al. (2001). The phases of low eddy energies are characterized by the quasi-antisymmetric circulation (see Fig. 3(a)), whereas the phases of high eddy energies are characterized by the asymmetric flow pattern (see Fig. 3(b)). Note that eddy energies are used to analyze the transient behaviour of the ocean model. In terms of total energies the asymmetric regime is more energetic than the quasi-antisymmetric regime. This complex behaviour of the ocean circulation is induced by the spatial inhomogeneity of the stochastic wind stress forcing. The stochastic forcing appears to enable the system to reach the neighbourhood of an unstable fixed point that is not reached without the spatially inhomogeneous stochastic wind field. The unstable fixed point then acts to steer the model into a temporarily persistent regime.

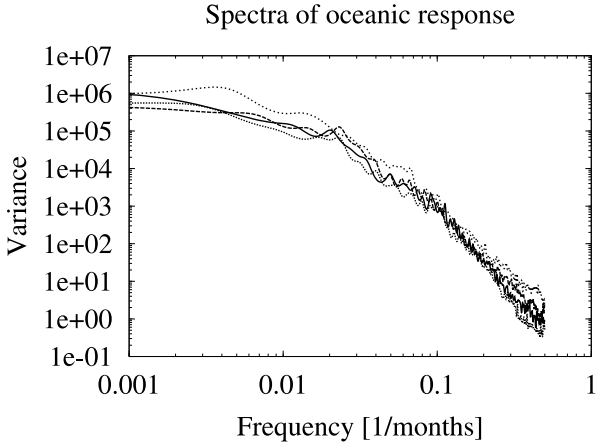

Fig. 4. Variance spectra of oceanic eddy kinetic energies for Model 1 (solid line), Model 2 (long dashed line), Model 3 (short dashed line), and Model 4 (dotted line).

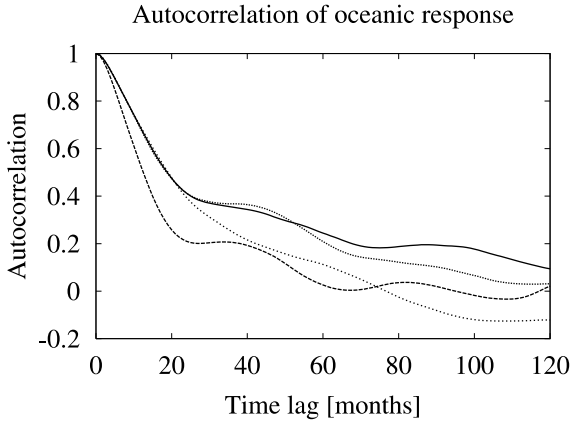

Fig. 5. Autocorrelation functions of oceanic eddy kinetic energies for Model 1 (solid line), Model 2 (long dashed line), Model 3 (short dashed line), and Model 4 (dotted line).

The spectra of the eddy kinetic energy time-series are shown in Fig. 4. In all experiments an overall red-noise behaviour is observed, as expected from the stochastic climate scenario proposed by Hasselmann (1976). The red oceanic spectrum is a consequence of the amplification of low-frequency weather fluctuations. Nevertheless, compared to Models 1 and 2, the oceanic spectrum forced by Model 3 shows an enhanced variability in the high-frequency range up to approximately 5 months, and enhanced low-frequency variability on timescales above approximately 50 months. The spectra of Models 1 and 2 are more similar. In summarizing the oceanic response in the spectral domain, it is worth mentioning that the low-frequency variability of the ocean model changes due to the different sampling techniques of the stochastic forcing. In particular, the oceanic low-frequency variability is somewhat enhanced if a pure red-noise forcing is used (Model 3). This is a consequence of the higher variability above the *e*-folding timescale of Model 3, compared to the spectra of Models 1 and 2 (see Fig. 1).

The stationary nature of the histograms in Fig. 2 and the spectra in Fig. 4 may mislead one into believing that the details of the stochastic forcing are irrelevant to the ocean response. An indication that this may not be the case is shown in Fig. 5. There, the autocorrelation functions of the eddy kinetic energy time-series are shown. The maximum time lag is set to 120 months, to reveal

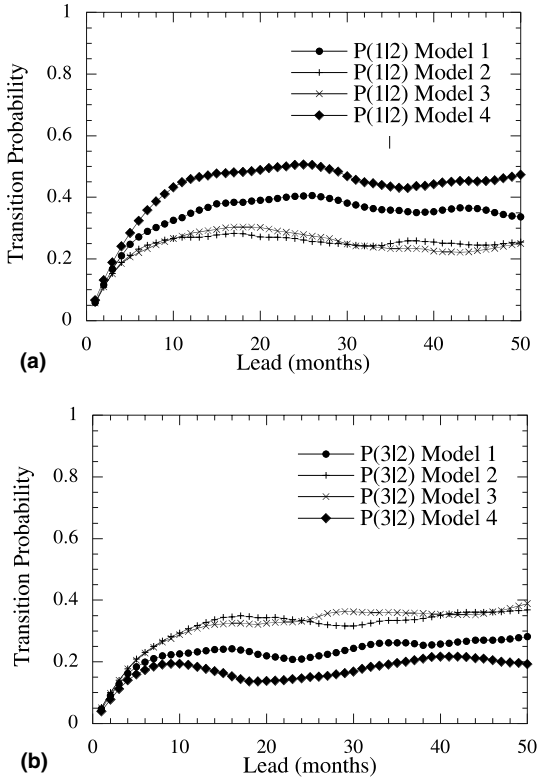

Fig. 6. Transition probabilities $p(i|2),\ i = 1, 3$, of going from the normal tercile (a) to the below normal state ($p(1|2)$) and (b) to the above normal state ($p(3|2)$) for Model 1 (filled circles). Model 2 (+-signs). Model 3 ($\times$-signs), and Model 4 (filled diamonds).

the rapidly-varying, that is in this case the monthly variability of the ocean model. The common feature in the oceanic response in all the stochastic models is that the main decorrelation time-scale, roughly defined as the width of the region with the steepest gradient, of the stochastically forced ocean is about 20–24 months. In that region the autocorrelation functions of the response to Model 1 and to Model 3 have nearly the same gradient. Only the ocean response in Model 2 has a somewhat steeper gradient. The autocorrelation of Model 1 remains the highest of all three stochastic models for time lags larger than 20–24 months. This behaviour of Model 1 is perhaps due to the fact that Model 1 forces regime transitions less often than Models 2 and 3. That is,

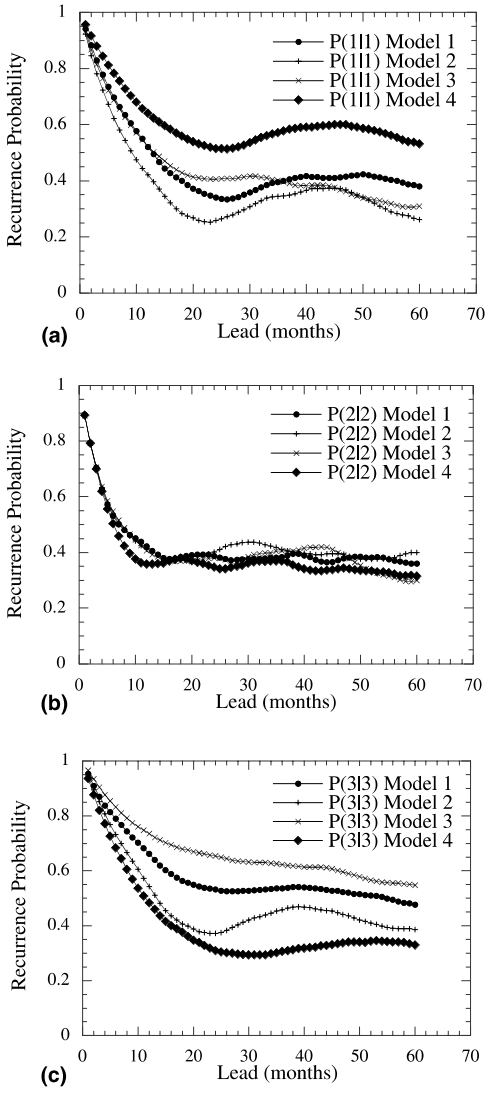

Fig. 7. Recurrence probabilities $p(i|i)$ that the system in state i will again (or still) be in state i some time later: (a) $i = 1$, (b) $i = 2$, and (c) $i = 3$. Symbols as in Fig. 6.

pronounced and frequent stochastically forced regime transitions observed in Models 2 and 3 result in a relatively low autocorrelation for time lags larger than the main decorrelation timescale.

The importance of exactly how the stochastic forcing is implemented is best considered using transition probabilities. For this calculation, we use Model 1 (Sura et al., 2001) as the control run. The corresponding histogram in Fig. 2 is divided into terciles, defining (1) "below normal", (2) "normal", and (3) "above normal". These same states are used for each of the three models. In each case, we estimate the conditional probability $p(i|j)$ that the system already in state j will undergo a transition to state i at some lead time τ, with $i, j = 1, 2, 3$. The transition probability of going from the center tercile to an extreme tercile as a function of lead time is shown in Fig. 6. The transition probabilities $p(i|2),\ i = 1, 3$, estimated from Models 2 and 3, are significantly different from those estimated from Model 1 at the 95% significance level for lead times greater than 6 months. Significance was assessed using the null hypothesis that the sampling populations were the same, and that differences of estimated probabilities were normally distributed (Spiegel, 1975). From Fig. 6 it is clear that the distribution of the driving noise plays a crucial role in the frequency of the transitions. The recurrence probability $p(i|i),\ i = 1, 2, 3$, that the system in state i will again (or still) be in state i some time τ later is shown in Fig. 7 for all three models. All visible differences are significant. While there may be some claim that the details of the stochastic forcing are not crucial to the probabilistic description of the normal state, both the distribution and the spectrum of the stochastic forcing are very important to the probabilistic description of the extreme states.

4.2. Model 4

Recall that the daily sampling of the stochastic wind forcing results in a reduced variance of the wind stress above the decorrelation timescale. Because of this the fourth experiment (Model 4), similar to Model 3, but with the total variance reduced to 12.5 $m^2\ s^{-2}$ is performed. The same tools as before are used to analyze the outcome of Model 4.

The time-series of eddy energies and the histogram the eddy kinetic energy (Fig. 2) reveals that the decrease of the total variance reduces the tendency of the system to adopt the asymmetric high eddy energy state. Obviously the total variance of stochastic forcing is not strong enough to enable the system to reach the neighbourhood of the unstable fixed point. Again, the spectra of the eddy kinetic energy time-series (Fig. 4) shows an overall red-noise behaviour. Nevertheless, the oceanic spectrum forced by Model 4 shows nearly the same low-frequency variability on timescale above about 50 months as the spectra of Models 1 and 2. The autocorrelation function of the eddy kinetic energy time-series of Model 4 is comparable to Model 1 (Fig. 5). The transition probabilities $p(i|2),\ i = 1, 3$, (Fig. 6) estimated from Model 4 are significantly different from those estimated from Models 1–3 at the 95% significance level for lead times greater than 6 months. Moreover, the recurrence probability $p(i|i),\ i = 1, 2, 3$, (Fig. 7) for Model 4 that the system in state i will again (or still) be in state i some time τ later is significantly different from the remaining three stochastic models.

Thus, Model 4 proves that the differences in the oceanic response for Models 1–3 are not due mainly to the higher amplitude noise in the white part of the forcing spectrum. Therefore, the long timescale behaviour of the double-gyre model indeed depends on the short timescale aspects of the stochastic forcing.

5. Summary and discussion

In this paper, we have illustrated in the context of a reduced gravity double-gyre ocean model driven by wind stress how "minor" details of stochastic forcing can have a significant effect on the temporal and spatial response by the forced system: The regime behaviour of the double-gyre model depends on the short-scale temporal aspects of the stochastic forcing.

These findings are important because the traditional education of geophysicists places a great deal of emphasis on how processes at different timescales may be studied in isolation from each other. While this approach is indeed useful in many cases, its application to nonlinear stochastic systems is ambiguous. In this study, we have examined a system which is neither linear nor deterministic. Our results show how physical processes in the ocean–atmosphere system with widely disparate timescales can and do interact. Further, we have shown that the distribution of the forcing in phase space can also be crucially important to the dynamical response of the system at long timescales. The implication is that details of stochastic forcing in a numerical climate model must be physically justified to the fullest extent possible.

In most cases of climatological interest, the stochastic forcing is intended to represent a combination of unresolved dynamical mechanisms. It is thus reasonable to invoke the CLT and assume the stochastic forcing to be normally distributed. The distribution, however, will not give accurate statistics if the timescales of the stochastic forcing are misrepresented.

The idea of stochastic forcing (particularly white stochastic forcing) having timescales may seem contradictory. The resolution of this apparent contradiction lies in the fact that continuous white noise is an idealization of a rapidly varying process which decorrelates much faster than the physical system it forces. That is, white noise represents a limiting case of vanishing correlation time and a simultaneous explosion of amplitude; the problem is that this limit depends on the spectral properties of the forcing at infinitesimal Fourier frequency resolution. Infinitesimal frequency resolution and infinite forcing amplitude are not realizable situations; it is a combination of the size and spectrum of the forcing which allows or disallows the white-noise approximation.

If any frequency information about the stochastic forcing can be gleaned from observations, then the correct stochastic limit is to be performed as in, for example, Kohler and Papanicolaou (1977). Otherwise, the simplest realistic assumption is to assume that the rapidly varying forcing decorrelates exponentially with some characteristic decay time. Naturally, this decay time may be very uncertain if it is smaller than the sampling time of an observed or numerically generated system. However, if the physical forcing is to be treated as stochastic in a numerical model, less violence is done to the long-time variability of the generated system by using some uncertain but finite decay time than by making grosser approximations to the stochastic forcing.

The implications of our results for long-range ensemble forecasting are clear: the accurate prediction of extreme events on seasonal to interannual timescales can strongly depend upon the representation of rapidly varying, perhaps unresolved, processes in a numerical prediction model. After all, stochastic processes are the macroscopic manifestation of unresolved nonlinear interactions. As stochastic parameterizations become popular (e.g., Buizza et al., 1999; Palmer, 2001), the accuracy of probabilistic forecasts will increasingly depend on how appropriate the stochastic representation is to the physical process it is meant to represent, despite the fact that ensemble weather forecasting does take an average of the ensemble members to improve the forecast. The dynamical form the CLT (Papanicolaou and Kohler, 1974; Sardeshmukh et al., 2001) offers some

guidance for doing this. As implied by this theorem, a stochastic description of a system is never arbitrary. On the contrary, as we have shown in the examples here, the timescales and distributions of stochastic parameterizations must be constructed in such a way that fidelity to the underlying dynamics is preserved. Therefore, further research is required to study carefully the response of more complex models (for example, a double-gyre ocean model with a substantially better resolution) to stochastic parameterizations.

Acknowledgements

We would like to thank Klaus Fraedrich for helpful discussions and support. Part of this work and a visit of CP to Hamburg was supported by the Deutsche Forschungsgemeinschaft within Sonderforschungs-bereich 512. Additional support by the Office of Naval Research is gratefully acknowledged. This paper was completed while PS was funded through the NASA Ocean Vector Science Team, JPL Contract number 1222984.

Appendix A. The spectra of the stochastic forcing models

Let us first consider the spectrum of a variable which is constant in the interval $[-T_0, T_0)$. That is, $x = a$ for $-T_0 \leqslant t < T_0$ and $x = 0$ otherwise.

Now, the corresponding Fourier transform reads

$$x(t) = \sum_n A_n \exp(\mathrm{i}\omega_n t)$$

or equivalently

$$\int_{-\infty}^{\infty} x(t) \exp(\mathrm{i}\omega_m t)\,\mathrm{d}t = \sum_n \int_{-\infty}^{\infty} A_n x(t) \exp(\mathrm{i}(\omega_n - \omega_m)t)\,\mathrm{d}t.$$

That is,

$$\left(\frac{a}{-\mathrm{i}\omega_m}\right)(\exp(-\mathrm{i}\omega_m T_0) - \exp(\mathrm{i}\omega_m T_0)) = 2\pi A_m$$

or

$$A_m = \left(\frac{a}{\pi\omega_m}\right)\sin(\omega_m T_0).$$

Hence,

$$x(t) = \sum_n \left(\frac{a}{\pi\omega_n}\right)\sin(\omega_n T_0)\exp(\mathrm{i}\omega_n t).$$

For a time-series $m \in E[0, \infty)$ this reads

$$x(t) = \sum_n \left(\frac{a_m}{\pi\omega_n}\right)\sin\left(\frac{\omega_n(t_{m+1} - t_m)}{2}\right)\exp(\mathrm{i}\omega_n t),$$

where $t_m \leqslant t < t_{m+1}$. Furthermore, for evenly spaced m this equation becomes

$$x(t) = \sum_n \left(\frac{a_m}{\pi\omega_n}\right) \sin\left(\frac{\omega_n \Delta}{2}\right) \exp(\mathrm{i}\omega_n t).$$

As a function of frequency ω_n this becomes

$$|x(\omega_n)|^2 = \left(\frac{a_m}{\pi\omega_n}\right)^2 \sin^2\left(\frac{\omega_n \Delta}{2}\right)$$

and

$$\langle |x(\omega_n)|^2 \rangle = \int_\Omega \left(\frac{a_m}{\pi\omega_n}\right)^2 \sin^2\left(\frac{\omega_n \Delta}{2}\right) \mathrm{d}P(a_m),$$

where the range of the integral is taken over the phase space of the distribution of a_m, that is, $\mathrm{d}P(a_m)$. For a flat distribution (Model 1) over the interval $[-\eta_0, \eta_0]$, $\mathrm{d}P(a_m) = \mathrm{d}a_m/(2\eta_0)$, and

$$\langle |x(\omega_n)|^2 \rangle = \frac{1}{3}\left(\frac{\eta_0}{\pi\omega_n}\right)^2 \sin^2\left(\frac{\omega_n \Delta}{2}\right). \tag{A.1}$$

If the distribution of a_m is Gaussian (Model 2) with standard deviation σ_0

$$\mathrm{d}P(a_m) = \frac{1}{\sqrt{2\pi\sigma^2}} \exp\left(\frac{-a_m^2}{2\sigma^2}\right) \mathrm{d}a,$$

the variance spectrum reads

$$\langle |x(\omega_n)|^2 \rangle = \left(\frac{\sigma_0}{\pi\omega_n}\right)^2 \sin^2\left(\frac{\omega_n \Delta}{2}\right). \tag{A.2}$$

Furthermore, if the variable $x(t)$ is generated with an univariate Ornstein–Uhlenbeck process, the Fourier transform of the corresponding autocorrelation function (13) yields the spectrum of Model 3:

$$\langle |x(\omega_n)|^2 \rangle = \frac{Q}{(2\pi)^2} \frac{1}{\omega^2 + \gamma^2}. \tag{A.3}$$

Note that the spectra of Models 1 and 2 [(A.1) and (A.2)] are identical, because the variance of a flat distribution in the interval $[-\eta_0, \eta_0]$ is $(2\eta_0)^2/12$. Graphs of the different spectra are shown in Fig. 1. It can be seen that the spectra of the distributions sampled once daily dip to zero at specific frequencies. This happens because waves interfere in order to find Fourier components which reproduce a perfect square wave.

References

Barnett, T.B., Pierce, D.W., Saravanan, R., Schneider, N., Dommenget, D., 1999. Origins of the mildlatitude Pacific decadal variability. Geophys. Res. Lett. 26, 1453–1456.

Blaauboer, D., Komen, G.J., Reiff, J., 1982. The behaviour of the sea surface temperature (SST) as a response to stochastic latent- and sensible heat forcing. Tellus 34, 17–28.

Buizza, R., Miller, M.J., Palmer, T.N., 1999. Stochastic simulation of model uncertainties in the ECMWF ensemble prediction system. Quart. J. Roy. Meteorol. Soc. 125, 2887–2908.

Cessi, P., Ierley, G.R., 1995. Symmetry-breaking multiple equilibria in quasi-geostrophic, wind-driven flow. J. Phys. Oceanogr. 25, 1196–1205.

Czaja, A., Frankignoul, C., 1999. Decadal buoyancy forcing in a simple model of the subtropical gyre. J. Phys. Oceanogr. 29, 3145–3159.

Farrell, B., Iaonnou, P., 1996a. Generalized stability theory: Part I. Autonomous operators. J. Atmos. Sci. 53, 2025–2040.

Farrell, B., Iaonnou, P., 1996b. Generalized stability theory: Part II. Non-autonomous operators. J. Atmos. Sci. 53, 2041–2053.

Frankignoul, C., Hasselmann, K., 1977. Stochastic climate models. Part II. Application to sea-surface temperature anomalies and thermocline variability. Tellus 29, 289–305.

Gardiner, C.W., 1985. Handbook of Stochastic Methods for Physics, Chemistry and the Natural Science, second ed. Springer, Berlin, 442 pp.

Griffa, A., Castellari, S., 1991. Nonlinear general circulation of an ocean model driven by wind with a stochastic component. J. Mar. Res. 49, 53–73.

Haidvogel, D.B., McWilliams, J.C., Gent, P.R., 1992. Boundary current separation in a quasi-geostrophic, Eddy-resolving ocean circulation model. J. Phys. Oceanogr. 22, 882–902.

Hasselmann, K., 1976. Stochastic climate models. Part I. Theory. Tellus 28, 473–484.

Horsthemke, W., Lefever, R., 1984. Noise-Induced Transitions: Theory and Applications in Physics, Chemistry, and Biology. Springer, Berlin, 318 pp.

Jiang, S., Jin, F.-F., Ghil, M., 1995. Multiple equilibria, periodic and aperiodic solutions in a wind-driven, double-gyre, shallow-water model. J. Phys. Oceanogr. 25, 764–786.

Junge, M., von Storch, J.-S., Oberhuber, J., 2000. Large-scale variability of the main thermocline excited by stochastic wind stress forcing. J. Climate 12, 2833–2840.

Kloeden, P., Platen, E., 1992. Numerical Solution of Stochastic Differential Equations. Springer, Berlin, 632 pp.

Kohler, W., Papanicolaou, G., 1977. Wave propagation in a randomly inhomogeneous ocean. In: Keller, J., Papadakis, J. (Eds.), Springer Lecture Notes in Physics, vol. 10. Springer, Berlin.

Mikolajewicz, U., Maier-Reimer, E., 1990. Internal secular variability in an ocean general circulation model. Climate Dyn. 4, 145–156.

Moore, A.M., 1999. Wind-induced variability of ocean gyres. Dyn. Atmos. Oceans 29, 335–364.

Münnich, M., Latif, M., Venske, S., Maier-Reimer, E., 1998. Decadal oscillations in a simple coupled model. J. Climate 11, 3309–3319.

Palmer, T.N., 2001. A nonlinear dynamical perspective on model error: a proposal for non-local stochastic-dynamic parametrization in weather and climate prediction models. Quart. J. Roy. Meteorol. Soc. 127, 279–304.

Papanicolaou, G., Kohler, W., 1974. Asymptotic theory of mixing stochastic ordinary differential equations. Commun. Pure Appl. Math. 27, 641–668.

Paul, W., Baschnagel, J., 1999. Stochastic Processes: From Physics to Finance. Springer, Berlin, 231 pp.

Pedlosky, J., 1996. Ocean Circulation Theory. Springer, Berlin, 453 pp.

Penland, C., Matrosova, L., 1994. A balance condition for stochastic numerical models with application to El Nino – the southern oscillation. J. Climate 7, 1352–1372.

Penland, C., Sardeshmukh, P.D., 1995. The optimal growth of tropical sea surface temperature anomalies. J. Climate 8, 1999–2024.

Primeau, F.W., 1998a. Multiple equilibria and low-frequency variability of wind-driven ocean models. PhD thesis, Massachusetts Institute of Technology, Woods Hole Occeanographic Institution, 158 pp.

Primeau, F.W., 1998b. Multiple equilibria of a double-gyre ocean model with super-slip boundary conditions. J. Phys. Oceanogr. 28, 2130–2147.

Rümelin, W., 1982. Numerical treatment of stochastic differential equations. SIAM J. Numer. Anal. 19, 604–613.

Saravanan, R., McWilliams, J.C., 1997. Stochasticity and spatial resonance in interdecadal climate fluctuations. J. Climate 10, 2299–2320.

Saravanan, R., McWilliams, J.C., 1998. Advective ocean–atmosphere interaction: an analytical stochastic model with implications for decadal variability. J. Climate 11, 165–188.

Sardeshmukh, P., Penland, C., Newman, M., 2001. Rossby waves in a fluctuating medium. In: Imkeller, P., von Storch, J.-S. (Eds.), Progress in Probability, Vol. 49: Stochastic Climate Models. Birkhäuser Verlag, Basel.

Scott, R.B., Straub, D.N., 1998. Small viscosity behaviour of a homogeneous quasi-geostrophic, ocean circulation model. J. Mar. Res. 56, 1225–1258.

Speich, S., Dijkstra, H., Ghil, M., 1995. Successive bifurcations in a shallow-water model applied to the wind-driven circulation. Nonlinear Process. Geophys. 2, 241–268.

Spiegel, M.R., 1975. Probability and Statistics. McGraw-Hill, New York, 372 pp.

Sura, P., Fraedrich, K., Lunkeit, F., 2001. Regime transitions in a stochastically forced double-gyre model. J. Phys. Oceanogr. 31, 411–426.

Sura, P., Lunkeit, F., Fraedrich, K., 2000. Decadal variability in a simplified wind-driven ocean model. J. Phys. Oceanogr. 30, 1917–1930.

Weng, W., Neelin, J.D., 1998. On the role of ocean–atmosphere interaction in midlatitude interdecadal variability. Geophys. Res. Lett. 25, 167–170.

Wright, P.B., 1988. An atlas based on the COADS data set: fields of mean wind, cloudiness and humidity at the surface of the global ocean. Technical Report 14, Max-Planck-Institut für Meteorologic, 68 pp. Available from Max-Plank-Institut für Meteorologic, Bundesstrasse 55, D-20146 Hamburg, Germany.